

# A Prognostic-Stochastic and Scale-Adaptive Cumulus Convection Closure for Improved Tropical Variability and Convective Gray-Zone Representation in NOAA's Unified Forecast System (UFS)

LISA BENGTSSON<sup>1</sup>,<sup>a</sup> LUC GERARD,<sup>b</sup> JONGIL HAN,<sup>c</sup> MARIA GEHNE,<sup>a,d</sup> WEI LI,<sup>e</sup> AND JULIANA DIAS<sup>a</sup>

<sup>a</sup> NOAA/ESRL/Physical Sciences Laboratory, Boulder, Colorado

<sup>b</sup> Royal Meteorological Institute, Brussels, Belgium

<sup>c</sup> NOAA/NCEP/Environmental Modeling Center, College Park, Maryland

<sup>d</sup> Cooperative Institute for Research in Environmental Sciences, University of Colorado Boulder, Boulder, Colorado

<sup>e</sup> I.M. Systems Group, NOAA/NCEP/ Environmental Modeling Center, College Park, Maryland

(Manuscript received 25 April 2022, in final form 25 August 2022)

**ABSTRACT:** A prognostic closure is introduced to, and evaluated in, NOAA's Unified Forecast System. The closure addresses aspects that are not commonly represented in traditional cumulus convection parameterizations, and it departs from the previous assumptions of a negligible subgrid area coverage and statistical quasi-equilibrium at steady state, the latter of which becomes invalid at higher resolution. The new parameterization introduces a prognostic evolution of the convective updraft area fraction based on a moisture budget, and, together with the buoyancy-driven updraft vertical velocity, it completes the cloud-base mass flux. In addition, the new closure addresses stochasticity and includes a representation of subgrid convective organization using cellular automata as well as scale-adaptive considerations. The new cumulus convection closure shows potential for improved Madden–Julian oscillation (MJO) prediction. In our simulations we observe better propagation, amplitude, and phase of the MJO in a case study relative to the control simulation. This improvement can be partly attributed to a closer coupling between low-level moisture flux convergence and precipitation as revealed by a space–time coherence spectrum. In addition, we find that enhanced organization feedback representation and stochastic effects, represented using cellular automata, further enhance the amplitude and propagation of the MJO, and they provide realistic uncertainty estimates of convectively coupled equatorial waves at seasonal time scales. The scale-adaptive behavior of the scheme is also studied by running the global model with 25-, 13-, 9-, and 3-km grid spacing. It is found that the convective area fraction and the convective updraft velocity are both scale adaptive, leading to a reduction of subgrid convective precipitation in the higher-resolution simulations.

**KEYWORDS:** Convective parameterization; Cumulus clouds; Stochastic models

## 1. Introduction

Atmospheric cumulus convection plays a key role in Earth's atmosphere's general circulation as it contributes to the vertical transport of heat, moisture, momentum and tracers, and via diabatic processes, associated with cloud formation and precipitation, impacts the stability of the atmosphere, and contributes to the hydrological cycle. In the tropics, the weather is dominated by atmospheric convection that interacts with larger-scale tropical waves. Such convectively coupled equatorial waves can span a few days, for instance Kelvin waves and inertia–gravity waves, up to a several weeks such as equatorial Rossby waves and the Madden–Julian oscillation (MJO). These equatorial disturbances drive tropical variability (Kiladis et al. 2009; Zhang 2005) and are important to weather prediction also outside of the tropics, since they affect remote weather through tropical to extratropical teleconnections (e.g., Schreck et al. 2013; Jones et al. 2011; Dias et al. 2021). In numerical weather predictions (NWP) of the atmosphere, the parameterization of cumulus convection largely influences the model's ability to accurately represent such tropical wave variability (e.g., Chikira and

Sugiyama 2010; Park 2014; Bengtsson et al. 2019b), where one important consideration is improved sensitivity to moisture in the troposphere within the cumulus parameterization. While the mechanism through which the convective parameterizations are sensitive to moisture may vary (e.g., through entrainment, closure, enhanced rain evaporation feedback, and convective initiation), idealized studies have demonstrated that moisture feedbacks are essential for convectively coupled equatorial wave initiation and propagation (Mapes et al. 2006). In addition, studies have shown that particularly the MJO is improved when convection is made more sensitive to environmental moisture (e.g., Maloney and Hartmann 2001; Benedict and Randall 2009; Tulich and Mapes 2010; Hannah and Maloney 2011; Kim et al. 2012). Furthermore, a recent study by Liu et al. (2021) indicates that the MJO prediction is largely improved if shallow convection is not activated until a time composite of moisture convergence over grid box turns to positive.

In many operational weather prediction centers around the world, cumulus convection is parameterized using a one-dimensional (vertical) entraining–detrainning plume model to simulate the vertical heat, moisture, tracer and momentum transport, as well as cloud and precipitation effects, of all the active cloud updrafts within a model grid box, averaged over different stages of their life cycle. The original concept of such a bulk mass-flux theory stems from the work of Yanai et al.

Corresponding author: Lisa Bengtsson, lisa.bengtsson@noaa.gov

(1973) and Arakawa and Schubert (1974), and is based on the assumption that the area coverage of all the cloud elements in a grid box is much smaller than the grid box itself, such that the average effect of the full ensemble of possible cloud elements in the grid box is in quasi-equilibrium with the resolved large-scale variables at any instant (steady-state assumption). However, this underlying assumption of a negligible area coverage, and statistical quasi-equilibrium at steady state, becomes problematic when the numerical model resolution increases, as individual cloud elements can cover a significant part of the grid box. In this cumulus convective *gray-zone* (Dorrestijn et al. 2013; Honnert et al. 2011), in which individual cumulus clouds are not resolved by the model dynamics, but the grid box is not large enough to support a statistical approach, it is suggested that the area fraction may no longer be neglected (e.g., Gerard et al. 2009; Gerard 2015; Arakawa and Wu 2013) and that the subgrid-scale variability of the different cloud updrafts should be sampled, rather than represented by an ensemble mean (e.g., Plant and Craig 2008; Plant et al. 2015; Monahan and Culina 2011; Bengtsson et al. 2019a).

NOAA's operational Global Forecast System (GFSv16) is currently using ~13-km grid spacing for deterministic medium range weather forecasts, the next upgrade to the model is envisioned to be fully coupled as the global model application of NOAA's Unified Forecast System (UFS). Therefore, we are fast approaching grid scales at which global operational model systems enter the gray-zone of cumulus convection.

Thus, the aim of this study is twofold:

- 1) to propose updates to the model's cumulus convection scheme that deviate from the steady-state quasi-equilibrium assumption, to better simulate cumulus convection at these higher resolutions. To this goal, a new cumulus convection closure is developed that exhibits stochasticity, prognostic evolution, and scale awareness.
- 2) to introduce moisture sensitivity and convective organization (three-dimensional considerations using cellular automata) to the convection scheme via the newly proposed prognostic closure, with the goal of better simulating the coupling between convection and large-scale circulation.

## 2. Further considerations about convective parameterizations

### a. Prognostic evolution and moisture sensitivity

Under the assumption of negligible area coverage (large grid boxes), the convective mass-flux profile is assumed to be parameterized as the balance between environmental air entrainment, and in-cloud detrainment along the edges of the updraft in a single steady state plume model. Thus, the impact of increased or reduced area coverage in a grid box is not explicitly described. If we no longer make the assumption that the area coverage is negligible, then the mass flux can be described directly as  $M = -(\sigma\omega_u/g)$ , where  $M$  is the mass-flux profile,  $\omega_u$  is the updraft velocity in pressure coordinates, and

$\sigma$  is the updraft area fraction. Under this formulation, a description of convective area fraction has to be provided, either using a constant approximated value, a statistical method (e.g., Dorrestijn et al. 2015; Gottwald et al. 2016), or a physical equation (e.g., Gerard and Geleyn 2005; Gerard et al. 2009; Gerard 2015).

Gerard and Geleyn (2005), Gerard et al. (2009) and Gerard (2015), use a prognostic equation for the updraft area fraction, expressed in terms of a moisture budget, where the area fraction increases in areas of large moisture flux convergence, and decreases as the moisture content is converted into cloud condensate, detrained to the environment and precipitated out as rain. The closure is part of a cumulus convection parameterization, called 3MT, that has been successfully used to represent convection at gray zone resolutions in the European regional numerical weather forecast model ALARO (Termonia et al. 2018). Some observational evidence is supportive of the assumption that the convection becomes stronger with increased area fraction, which is the key assumption in the formulation of the mass flux at cloud base in the present study. Furthermore, there is some evidence that the area fraction is related to strong moisture flux convergence, which is in turn the underlying assumption in our proposed formulation of the prognostic updraft area fraction. For instance, Louf et al. (2019) used a C-band dual-polarimetric radar at Darwin, Australia, in order to provide guidance of the relationships between convective ensembles and their large-scale environment. They found that the area-mean convective rainfall in a convective region is largely determined by the area that is raining. A similar conclusion is reached in Schiro et al. (2020), who used multiple independent satellite and reanalysis datasets to study the relationship between precipitation intensity and the mesoscale convective system radius. They found that the maximum precipitation intensity linearly increases with increasing radius of the convective core as well as the whole total system. Furthermore, earlier observational analysis at Darwin, conducted by Davies et al. (2013), demonstrated that larger moisture convergence is associated with increased convective precipitation through, predominantly, increasing the convective precipitation area. Their study found that the correlation between convective precipitation area and moisture convergence was significantly larger than the correlation between convective precipitation area and convective available potential energy (CAPE).

Therefore, in this study, our starting point is to include the prognostic evolution of the updraft area fraction from Gerard et al. (2009) in the description of the convective closure assumption in NOAA's Unified Forecast System. This is done in order to deviate from the quasi-equilibrium assumption as we go to higher resolution, to improve the description of the convective life cycle, and to add moisture sensitivity to the closure of both shallow and deep convection. It should be noted, that the new closure does not take the place of a buoyancy-type closure, atmospheric instability is a crucial component for the initiation and strength of cumulus convection. The full closure is the product between updraft velocity (buoyancy driven) and the updraft area fraction (moisture driven).

### *b. Stochasticity and convective organization using cellular automata*

In addition to the fact that we can no longer assume negligible area fraction as the gridbox size is reduced, the standard deviation of the parameterized fluxes increases with decreasing gridbox size (e.g., [Dorrestijn et al. 2013](#)) and the plume distribution and area coverage, can vary vastly from one grid box to another. Hence, at higher resolution, the subgrid-scale variability should be sampled, rather than being represented by a gridbox mean value. To this end, a number of studies have explored whether stochastic approaches for deep convection can be used to address statistical fluctuations in cloud number, initiation or intensity (e.g., [Plant and Craig 2008](#); [Khouider et al. 2010](#); [Dorrestijn et al. 2013](#); [Gottwald et al. 2016](#); [Frenkel et al. 2013](#); [Bengtsson et al. 2013, 2019a, 2021](#); [Sakradzija et al. 2016](#); [Hagos et al. 2018](#)).

For longer range forecasts (seasonal, decadal, and climate scale), the relevance of stochastic cumulus convection in numerical models can also be discussed in terms of noise induced forcing. As an example, on the time scale of organized convectively coupled waves, the small-scale individual convective plumes grow and decay so rapidly that they are not predictable on time scales longer than a few hours (e.g., [Hohenegger and Schär 2007](#)), whereas the organized larger-scale convectively coupled wave envelope can have a deterministic limit of predictability of about two weeks ([Lorenz 1969](#)), or as long as 20 days if considering the tropical region alone ([Judt 2020](#)). Thus, for longer range forecasts, individual convective plumes can be viewed as stochastic noise—they can have an impact on the convectively coupled waves (due to noise forcing), but they are not predictable on their own.

In addition to a prognostic evolution of the area fraction, and the inclusion of stochastic effects, we also aim at representing the large-scale effects of subgrid organized convection. In nature, physical processes driving convective organization are complex, as the mechanisms are associated with small-scale physical processes as well as interaction with larger-scale waves ([Huang 1988](#); [Houze 2004](#); [Tompkins 2001](#); [Kiladis et al. 2009](#)). It has also been demonstrated using a cloud classification and tracking dataset ([Feng et al. 2021](#)) that mesoscale convective systems (MCSs) play a crucial role in the precipitation–moisture coupling over tropical oceans ([Chen et al. 2022](#)). In practice we seek to parameterize the effect of more convective organization (or aggregation), in such a way that the large scale would respond to more organization through e.g., stronger updraft or triggering in the nearby environment (e.g., [Mapes and Neale 2011](#); [Bengtsson et al. 2021](#); [Moncrieff et al. 2017](#); [Park 2014](#)).

In the current study, sensitivity to including a parameterization of convective organization using the properties of a stochastic self-organizing cellular automaton, following the methodology outlined in [Bengtsson et al. \(2021\)](#) is explored. The cellular automaton is conditioned on model variables known to control convective organization (in this study vertically integrated subgrid rain evaporation is used). In this way the cellular automaton provides a simple model for subgrid, and cross-grid, convective organization that can lead to the enhancement of the updraft

area fraction ([Bengtsson et al. 2013, 2021](#)). We use this information to enhance the area fraction provided by the new prognostic equation of the area fraction discussed above, in regions of strong subgrid or cross-grid organization modeled by the cellular automaton. Furthermore, as discussed in [Bengtsson et al. \(2019a\)](#), a prognostic equation including stochastic additive noise, will better represent upscale error growth, when compared with a local perturbation, because of dynamical memory of the uncertainty itself.

### *c. Scale adaptiveness*

Last, since the updraft area fraction is not only indicative of stronger or weaker convection, but is also a function of the gridbox size itself, we here study the behavior of the new prognostic and stochastic description of the area fraction at various resolutions of the global application of the UFS (GFS), ranging from 25-km grid spacing down to 3 km. The aim is for the area fraction to become larger with decreasing grid spacing, but at the same time reduce the strength of convection with decreasing grid spacing as more and more convection becomes resolved. To achieve this goal, we follow the methodology outlined in [Arakawa and Wu \(2013\)](#) and [Wu and Arakawa \(2014\)](#), as described in more detail in the methodology section next.

## 3. Methodology

### *a. Current cumulus convection closure in the GFS*

The version of the GFS used in this study is referred to as GFSv16, which is the version of the GFS currently used for operational medium range weather forecasts at NOAA. It is an uncoupled model in which sea surface temperatures are prescribed. In its operational configuration it uses the FV3 dynamical core (see, e.g., [Lin and Rood 1996](#); [Lin 2004](#); [Harris et al. 2016](#) and references therein) in nonhydrostatic mode, with 768 grid cells on a cube sphere tile (C768), which corresponds to a global horizontal resolution of about 13 km. It uses 127 vertical layers, and a model top at 80 km. GFSv16 uses a cloud microphysics scheme referred to as the GFDL microphysics ([Lin et al. 1983](#); [Chen and Lin 2013](#)), which is a one-moment bulk microphysics scheme using six prognostic water species. The planetary boundary layer (PBL) scheme is a scale-aware turbulent kinetic energy (TKE)-based Eddy-Diffusion Mass-Flux (TKE-EDMF) scheme ([Han and Bretherton 2019](#)). It utilizes an eddy diffusion mass flux (EDMF) approach where the local mixing by small turbulent eddies is modeled using a prognostic TKE and turbulent mixing length, and the nonlocal mixing by large convective plumes is modeled using a mass flux approach, following [Siebesma et al. \(2007\)](#). The deep cumulus parameterization is originally based on [Arakawa and Schubert \(1974\)](#) and [Grell \(1993\)](#), but has over the years seen substantial updates following [Pan and Wu \(1995\)](#), [Han and Pan \(2011\)](#), and [Han et al. \(2017\)](#). This deep cumulus scheme is referred to as the scale-aware simplified Arakawa–Schubert (saSAS). The scale-aware shallow cumulus scheme is based on [Han and Pan \(2011\)](#) and [Han et al. \(2017\)](#), employing a mass flux parameterization.

The current deep convection scheme in the GFS consists of two optional closure formulations. The first one, which is used in current operational GFS for medium range weather forecasts, computes the updraft mass flux at cloud base using the Arakawa–Schubert quasi-equilibrium assumption, where the area fraction is assumed to be much smaller than 1, and thus negligible:

$$M_{BE} = \frac{A - \alpha(\omega)A_0}{\tau} \frac{M'_B \delta t}{A' - A}, \quad (1)$$

$$A = \int_{Z_B}^{Z_T} \frac{g}{C_p T(z)} \frac{1}{1 + \beta} [h_u(z) - \bar{h}_s(z)] dz, \quad \text{and} \quad (2)$$

$$\beta = \frac{L}{C_p} \left( \frac{\partial \bar{q}}{\partial T} \right)_p. \quad (3)$$

Here  $M_{BE}$  is the equilibrium mass flux at the cloud base. Buoyancy is represented by the so-called cloud work function  $A$ . Note that, while  $A$  is still referred to as the “cloud work function” here, in practice it is more of a dilute convective available potential energy (CAPE) variant of the closure in that in-cloud values are used, and the formulation has deviated somewhat from the original Arakawa and Schubert (1974) formulation over the years; for example, there is no factor included for the vertical profile of normalized mass flux in the current formulation used in GFSv16. The  $A_0$  is a reference cloud work function derived from empirical studies by Lord (1978);  $\alpha(\omega)$  is a function of resolved vertical velocity,  $\omega$ , which is used to modify  $A_0$ ;  $\tau$  is a convective adjustment time scale, inversely proportional to the convective turnover time following Bechtold et al. (2014);  $A'$  is the cloud work function after the modification of the thermodynamic fields by an arbitrary amount of mass-flux  $M'_B \delta t$ ;  $T$  is the environmental temperature;  $C_p$  is the specific heat at constant pressure;  $L$  is the latent heat of the vaporization of water;  $h$  is the moist static energy of a parcel;  $q$  is the moisture; the subscripts  $u$  and  $s$  stand for updraft and saturation, respectively; the overbar represents the environmental mean value;  $z$  is the height; and  $Z_T$  and  $Z_B$  are the heights at the cloud top and base, respectively.

An alternative closure was introduced to the GFS deep convection scheme as outlined in Han et al. (2017), for grid sizes smaller than a threshold value (currently set to 8 km). In this closure the cloud-base mass flux in the deep convection scheme is given by a function of mean updraft velocity rather than by the Arakawa–Schubert quasi-equilibrium closure described above:

$$M_{BE} = 0.03 \bar{w}_u \rho, \quad (4)$$

where  $\bar{w}_u$  is the updraft velocity averaged over the whole cloud depth (indicated by the overbar) and  $\rho$  is density. The value 0.03 is essentially a scaling coefficient; however, it can be viewed as the “negligible” updraft area fraction at low resolution, at the base of a bulk updraft, in the case where the cloud base updraft velocity would be equal to the cloud

average updraft velocity in the model grid box. The updraft velocity  $w_u$  is computed following (Simpson and Wiggert 1969):

$$\partial w_u^2 / \partial z = -c_1 \varepsilon w_u^2 + c_2 B, \quad (5)$$

with the buoyancy  $B = g(\theta_{uu} - \bar{\theta}_v) / \bar{\theta}_v$  as a source term (where  $\theta_v$  is the virtual potential temperature and  $g$  is the gravity). The  $\varepsilon$  is the lateral entrainment rate, and the values of the coefficients,  $c_1$  and  $c_2$ , are given as 4.0 and 0.8, respectively. Importantly, Eq. (4) is also used for the mass flux at cloud base in the shallow convection scheme.

In the current GFS cumulus convection schemes (deep and shallow), scale awareness is considered by reducing the equilibrium mass flux at cloud base as a function of convective updraft area fraction  $\sigma_f$ , following the proposed framework of Arakawa and Wu (2013), such that the final cloud-base mass flux reads

$$M_B = (1.0 - \sigma_f)^2 M_{BE}. \quad (6)$$

However, different from Arakawa and Wu (2013), which derives the updraft area fraction from the ratio between the gridbox mean convective eddy transport, and the equilibrium mass flux (computed under the negligible updraft area fraction assumption), the GFS deep and shallow convection schemes use an updraft area fraction  $\sigma_f$  given by Grell and Freitas (2014), as

$$\sigma_f = 3.14 R_c^2 / A_{\text{grid}}, \quad (7)$$

where the radius of the convective updraft is  $R_c = 0.2 / \varepsilon_0$ , which uses the turbulent lateral entrainment rate of the updraft at the cloud-base height  $Z_B$ , which is  $\varepsilon_0(z_B) = c_0 / z_B$  (Han and Pan 2011), and the gridbox area  $A_{\text{grid}}$ . Since Eq. (6) is not a reasonable assumption in the low-resolution quasi-equilibrium regime, the control GFSv16 only applies the  $(1.0 - \sigma_f)^2$  scaling at grid sizes smaller than 15 km.

#### b. Proposed cumulus convection closure

In this study, to deviate from the quasi-equilibrium theory, we no longer assume negligible area fraction, and thus compute the mass flux at cloud base in a similar manner as Han et al. (2017), as given by Eq. (4), with the exception of replacing the constant estimate of the updraft area fraction (0.03), with a prognostic (and advected) physical equation inspired by the moisture budget equation given by Gerard and Geleyn (2005) and Gerard et al. (2009):

$$\frac{\partial \sigma_B}{\partial t} \int_{p_B}^{p_T} \xi(p) [h_u(p) - h_s(p)] \frac{dp}{g} = L \int_{p_B}^{p_T} \sigma_B \omega_u \xi(p) \frac{q_{\text{cond}}}{g} + L \int_{p_B}^{p_T} \text{MFC} \frac{dp}{g}. \quad (8)$$

Here the source term is the moisture flux convergence (MFC), which includes the moisture flux from microphysics, dynamics (advection and divergence), and turbulent moisture

flux (from the PBL scheme). The sink term is the moisture being converted into cloud condensation in the updraft. The  $\sigma_B$  is the updraft area fraction at cloud base,  $\omega_u$  is the updraft velocity in pressure coordinates (i.e.,  $\text{Pa s}^{-1}$ ),  $p_B$  and  $p_T$  represent the pressure at cloud base and cloud top, respectively,  $h_u$  is the moist static energy of the updraft,  $h_s$  is the saturation moist static energy,  $g$  is acceleration of gravity,  $L$  is the latent heat of vaporization, and  $\delta q_{\text{cond}} = (\partial q/\partial p)dp$  is the moisture being converted to cloud condensation in the updraft. The meaning of  $\xi(p)$  is discussed at a bit more length below.

In Gerard et al. (2009), the entire mass-flux profile is computed as  $M = -(\sigma_u \omega_u)/g$ , using the same updraft area fraction at each level  $\sigma_u(p) = \sigma_B$ , while  $\omega_u$  is computed with a prognostic equation at each model level. Thus, the mass flux at cloud base is consistent with the formulation of the mass-flux vertical profile. In our approach, we are only modifying the mass flux at cloud base in the existing convection schemes and are thus using a different definition of the mass flux in the closure integral in Eq. (8) and in the rest of the scheme (which computes the mass-flux profile based on entrainment minus detrainment). To be more consistent, we here compute a profile of the updraft area fraction  $\sigma_u(p) = \sigma_B \xi(p)$ , where  $\xi(p)$  is proportional to the vertically normalized mass-flux profile  $\eta(p)$ , derived using the relationship:

$$\begin{aligned} M(p) &= \sigma_B \xi(p) \omega_u(p) = M_B \eta(p) = \sigma_B \omega_b \eta(p) \\ \Rightarrow \xi(p) &= \eta(p) \frac{\omega_b}{\omega_u(p)}. \end{aligned} \quad (9)$$

Here,  $M_B$  is the mass flux at cloud base. Then  $\sigma_u(p) = \sigma_B \xi(p)$  is used in the closure integral Eq. (8) for consistency.

After combining Eqs. (4), (6), and (8) and replacing the area fraction  $\sigma_f$  with the new prognostic  $\sigma_B$ , the equation for the mass flux at cloud base reads

$$M_B = -(1.0 - \sigma_B)^2 \frac{\sigma_B \overline{\omega_u}}{g}. \quad (10)$$

The expectation is that the convective area fraction should increase with decreasing grid size, as a larger fraction of the grid box will be taken up by cumulus convection. At the same time, as we go toward higher resolution, more mesoscale motion will be resolved by the model, and the parameterized mass flux should thus decrease with decreasing grid size, to allow the model to resolve more vertical motions associated with convection. Thus, the global simulations using 3-km grid spacing are expected to have a reduction of convective precipitation, which is taken over by model-resolved precipitation.

### c. Enhanced organization using cellular automaton

In addition to the new prognostic closure formulation, we also explore the impact of representing subgrid-scale convective organization feedback and stochasticity represented by the self-organizing properties of cellular automata following Bengtsson et al. (2013), (2021). Consistent with the theory outlined in Mapes and Neale (2011) and Bengtsson et al. (2021), the updraft area fraction should increase as a consequence of more convective organization/aggregation. This

increase in area fraction leads to enhanced convective mass flux, increased subgrid precipitation, and consequently stronger subgrid evaporation and cooling from falling precipitation, which would further enhance organization (due to subgrid-scale cold pool dynamics). Thus, the impact of more organized subgrid clouds is a time-lagged but positive feedback on deep convection development (Mapes and Neale 2011).

The details of the stochastic and self-organizing cellular automaton implemented in the UFS (in the global application-GFS) can be found in Bengtsson et al. (2021). The evolution of the cellular automaton is an extension to the cellular automaton known as ‘‘Generations,’’ which is based on the ‘‘Game of Life’’ (Chopard and Droz 1998) but adds cell history to the rule set. This means that a newborn cell is given a lifetime that is incrementally reduced by 1 each time step where the rules are not met, in contrast to the binary state 1 or 0. The value of the lifetime is determined by the vertically integrated subgrid rain evaporation and is given a maximum time scale that depends on the model time step. The cellular automaton is evolved on a higher-resolution grid than the GFS model, such that the cells organize themselves into various clusters of differing scales on the subgrid. In Bengtsson et al. (2021), it was found beneficial to let the self-organizing properties of the cellular automaton inform the cumulus parameterization scheme of convective initiation in the nearby environment. It was demonstrated that the near gridscale precipitation autocorrelation and autocovariance become more consistent with observations, and that the interaction between convection and the large scales are improved. For example, the phase speed of eastward-propagating Kelvin waves better match the observed phase speeds. In this study, we explore the impact of letting the cellular automaton increase the updraft area fraction given by Eq. (8), in regions where the subgrid rain evaporation driven cellular automaton is exhibiting more self-organization. This is done by coarse-graining back the cellular automaton onto the GFS model grid, providing an area fraction representing more or less organization on the subgrid. This area fraction  $\sigma_{CA}$  is then simply added to the previously computed updraft area fraction given by Eq. (8), and the final mass flux at cloud base, if the cellular automata contribution is included, is given by

$$M_B = -(1.0 - \sigma_B - \sigma_{CA})^2 \frac{(\sigma_B + \sigma_{CA}) \overline{\omega_u}}{g}. \quad (11)$$

While  $\sigma_{CA}$  in individual grid boxes can be on the same order of magnitude as  $\sigma_B$ , the contribution to the total updraft area fraction by the cellular automaton is relatively small in the mean. This will be discussed in more detail in the next section.

Just as it is not reasonable to assume negligible convective area fraction at the high resolutions, it is not reasonable to let the convective area fraction consume the majority of the grid box in e.g., the 25-km run. To address this, upper level limits of the area fraction are provided in the scheme, such as  $\sigma_{BMAX} = (\sigma_{BMAX} \leq \alpha dx)$ , where  $\alpha = 7000$  m and  $dx$  is the gridbox length in meters. This way, the maximum value of the updraft area fraction is 0.28, 0.54, 0.78, and 1.0 for the 25-, 13-, 9-, and 3-km resolutions, respectively. Similar to the argument

TABLE 1. Description of the experiments conducted in this study.

Expt name	Description	Length of simulation	Resolution	Initial conditions
Control_low	GFSv16	90 days	C384 (~25 km)	19 Oct, 24 Oct, 29 Oct, 3 Nov, and 8 Nov 2019
Prog_low	GFSv16 with prognostic closure	90 days	C384 (~25 km)	19 Oct, 24 Oct, 29 Oct, 3 Nov, and 8 Nov 2019
Ca_low	GFSv16 with prognostic closure and cellular automata	90 days	C384 (~25 km)	19 Oct, 24 Oct, 29 Oct, 3 Nov, and 8 Nov 2019
Control_high	GFSv16	25 days	C768 (~13 km)	19 Oct 2019
Prog_high	GFSv16 with prognostic closure	25 days	C768 (~13 km)	19 Oct 2019
Prog_ca_high 5 members	GFSv16 with prognostic closure and cellular automata	25 days	C768 (~13 km)	19 Oct 2019
Control_25_short	GFSv16	24 h	C384 (~25 km)	19 Oct 2019
Prog_25_short	GFSv16 with prognostic closure	24 h	C384 (~25 km)	19 Oct 2019
Control_13_short	GFSv16	24 h	C768 (~13 km)	19 Oct 2019
Prog_13_short	GFSv16 with prognostic closure	24 h	C768 (~13 km)	19 Oct 2019
Control_9_short	GFSv16	24 h	C1152 (~9 km)	19 Oct 2019
Prog_9_short	GFSv16 with prognostic closure	24 h	C1152 (~9 km)	19 Oct 2019
Control_3_short	GFSv16	24 h	C3072 (~3 km)	19 Oct 2019
Prog_3_short	GFSv16 with prognostic closure	24 h	C3072 (~3 km)	19 Oct 2019

stated above [that Eq. (6) is not a reasonable assumption in the low-resolution quasi-equilibrium regime], this also applies for Eq. (11). Thus, the new formulation only applies the scaling  $(1.0 - \sigma_B - \sigma_{CA})^2$  at grid sizes smaller than 13 km.

#### 4. Experimental setup

The experiments conducted in this study are set up to assess the impact of the new deep and shallow convective closure on tropical variability, MJO prediction, as well as scale adaptiveness at gray-zone resolutions. Thus, we carry out model runs at lower resolution (~25 km), to be able to run seasonal simulations (90 days), for five sets of initial conditions ranging from 19 October to 3 December 2019, 5 days apart. This set of runs allow us to study the impact on the model seasonal mean state, wave propagation, space-time spectra and moisture coupling. In addition, we carry out 25-day simulations at the current operational higher resolution (~13 km) for an MJO case study, to investigate the model's ability to propagate and maintain an MJO event with and without the proposed new closure, as well as the impact of the feedback from more subgrid organization provided by the cellular automaton. Last, we run very high-resolution global simulations at ~9- and ~3-km resolution. These are only run out to 24 h because of the extremely high computational cost associated with the 3-km global run. A caveat with such short simulations could be that the model is still adjusting to an equilibrium state and spinup effects may still be visible. In these runs, we study the scale-adaptive behavior of the convective mass flux, convective and total precipitation, comparing the control with the new prognostic closure. Table 1 summarizes the set of experiments carried out in this study.

In all of the experiments we initialize the model for the atmosphere, land surface and sea surface temperature (SST) from preoperational model runs corresponding to GFSv16,

and SSTs are relaxed to a climatology on a time scale of 90 days to account for seasonality (as done in operations). There is no other stochastic parameterizations or effects included in these simulations besides the cellular automata.

In this study,  $\sigma_{CA}$  provides a relatively small increase to the domain mean updraft area fraction. The cellular automaton is, as such, a modest perturbation to the overall cloud-base mass flux, and therefore, does not substantially change the overall level of convective activity in the model as seen in the mean (Fig. 1). Figure 1 shows the equatorial mean time series of  $\sigma_B$ , and  $\sigma_B + \sigma_{CA}$ , from the prog\_low and the ca\_low experiments (as defined in Table 1), as well as the equatorial mean time series of convective precipitation ( $\text{mm day}^{-1}$ ) from the prog\_low and ca\_low experiments. Since  $\sigma_{CA}$  and  $\sigma_B$ , are computed independently in the ca\_low experiments, the terms can be diagnosed independently, even if it is the sum of  $\sigma_B + \sigma_{CA}$  that is used as the convective area fraction in the ca\_low experiment. This is shown as a time series of the tropical average ( $10^\circ\text{S}$ – $10^\circ\text{N}$ ) area fraction, for the 29 October 2019 initial condition, although the behavior is similar for all five different initial conditions defined in Table 1 (not shown). The,  $\sigma_B$  (orange) and  $\sigma_B + \sigma_{CA}$  (green) time series from the ca\_low experiment demonstrate that the impact of the cellular automaton means a small increase in the mean of the convective area fraction. If, instead,  $\sigma_B$  is compared between the ca\_low (orange) and prog\_low (blue) experiments, the nonlinear response in  $\sigma_B$  due to the cellular automaton addition can be studied. Doing so, it can be seen that  $\sigma_B$  in the ca\_low experiment diverges from  $\sigma_B$  in the prog\_low experiment in a nonsystematic way for longer lead times. This response is perhaps clearer when comparing the response in convective precipitation between the ca\_low and prog\_low experiments (bottom panel); the impact of the cellular automaton does not systematically increase convective precipitation. Thus, it is concluded that the main impact of the cellular automata

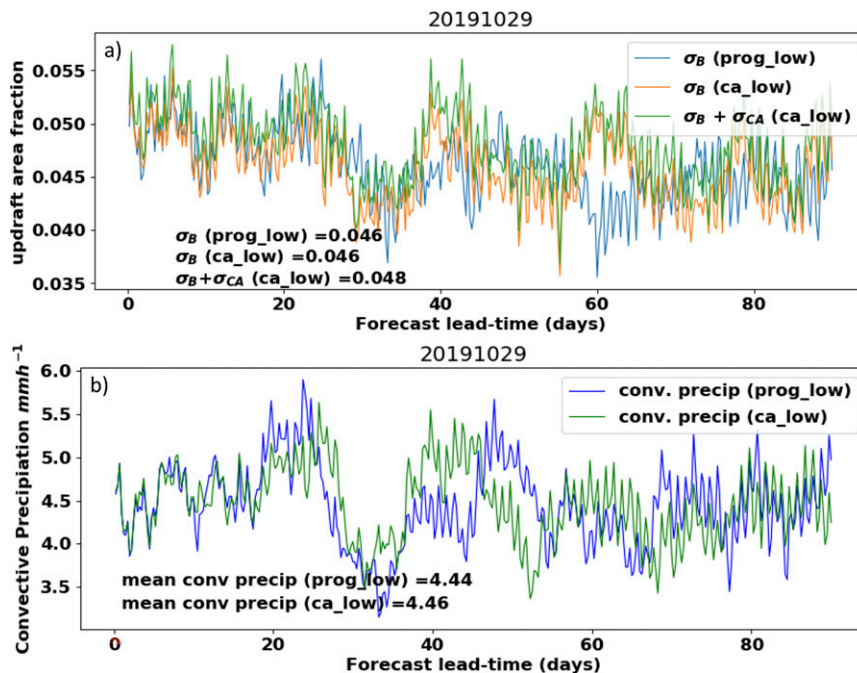


FIG. 1. (a) Updraft area fraction (tropical average  $10^{\circ}\text{S}$ – $10^{\circ}\text{N}$ ) as computed using the prognostic closure,  $\sigma_B$ , and cellular automata,  $\sigma_{CA}$ , from the prog\_low and ca\_low experiments. (b) Tropical average ( $10^{\circ}\text{S}$ – $10^{\circ}\text{N}$ ) convective precipitation ( $\text{mm day}^{-1}$ ) from the prog\_low and ca\_low experiments. The forecast is initialized at 29 Oct 2019.

serves as a noise induced forcing, as the systematic mean forcing is small. It is interesting to note, however, that a systematic response to the cellular automata inclusion is visible in the space–time coherence spectra between low-level moisture convergence and precipitation (section 5a), and to some extent in the MJO prediction shown in section 5c in terms of propagation, amplitude, and phase. This will be exemplified and discussed in the coming sections.

## 5. Results

### a. Tropical variability, seasonal simulations

The motivation for carrying out and analyzing seasonal simulations is to study the model’s ability to initiate and propagate convectively coupled equatorial waves at later lead times, when the influence of the initial state is reduced. The hypothesis is that there is a stronger coupling between low-level moisture convergence and precipitation in simulations using the new prognostic closure formulation, as the new closure is based on a prognostic moisture budget equation, in addition to the updraft velocity.

The precipitation mean state over the 90 days is averaged over the five separate initial conditions (Fig. 2) for the control, prog\_low, and ca\_low experiments. In general, the mean states between the three simulations are not vastly different. There is some enhanced precipitation along the convergence zones, in particular over the South Pacific convergence zone (SPCZ), in the prog\_low experiment relative to the control and ca\_low runs, which is an overestimate when compared

with ERA5 (Hersbach et al. 2020). The enhanced precipitation in the intertropical convergence zone (ITCZ) in the prog\_low and ca\_low experiments is generally more in line with the reanalysis. A reduction of precipitation over Brazil and an increase in precipitation over Colombia/Ecuador in the experiment is also more in agreement with the reanalysis. Neither of the hindcasts captures the mean precipitation amounts over the Indian Ocean that are present in the ERA5 reanalysis.

Table 2 summarizes the global and tropical ( $10^{\circ}\text{S}$ – $10^{\circ}\text{N}$ ) mean total and convective precipitation rates ( $\text{mm day}^{-1}$ ) for the three model simulations. While the changes in mean precipitation are relatively small, there is a tendency toward somewhat reduced convective precipitation and increased resolved precipitation in the prog\_low and ca\_low simulations when compared with the control as a *global* mean. However, over the *tropical band*, there is an increase in mean convective precipitation in particularly with the new closure, in particularly in the ca\_low experiment, from Fig. 2 it can be seen that this is mainly related to the enhanced precipitation over the ITCZ.

While the precipitation mean state does not show very large differences, the Hovmöller diagrams (Hovmöller 1949; Fig. 3) suggest large differences in the characteristics of the space–time organization of precipitation. Figure 3a illustrates how tropical precipitation in ERA5 reanalysis (averaged over the equatorial band  $5^{\circ}\text{S}$ – $5^{\circ}\text{N}$ ) is organized as coherent precipitating structures (convectively coupled equatorial waves) zonally propagating at different space–time scales. The panels in Figs. 3b–d show the 90-day forecasts of tropical precipitation

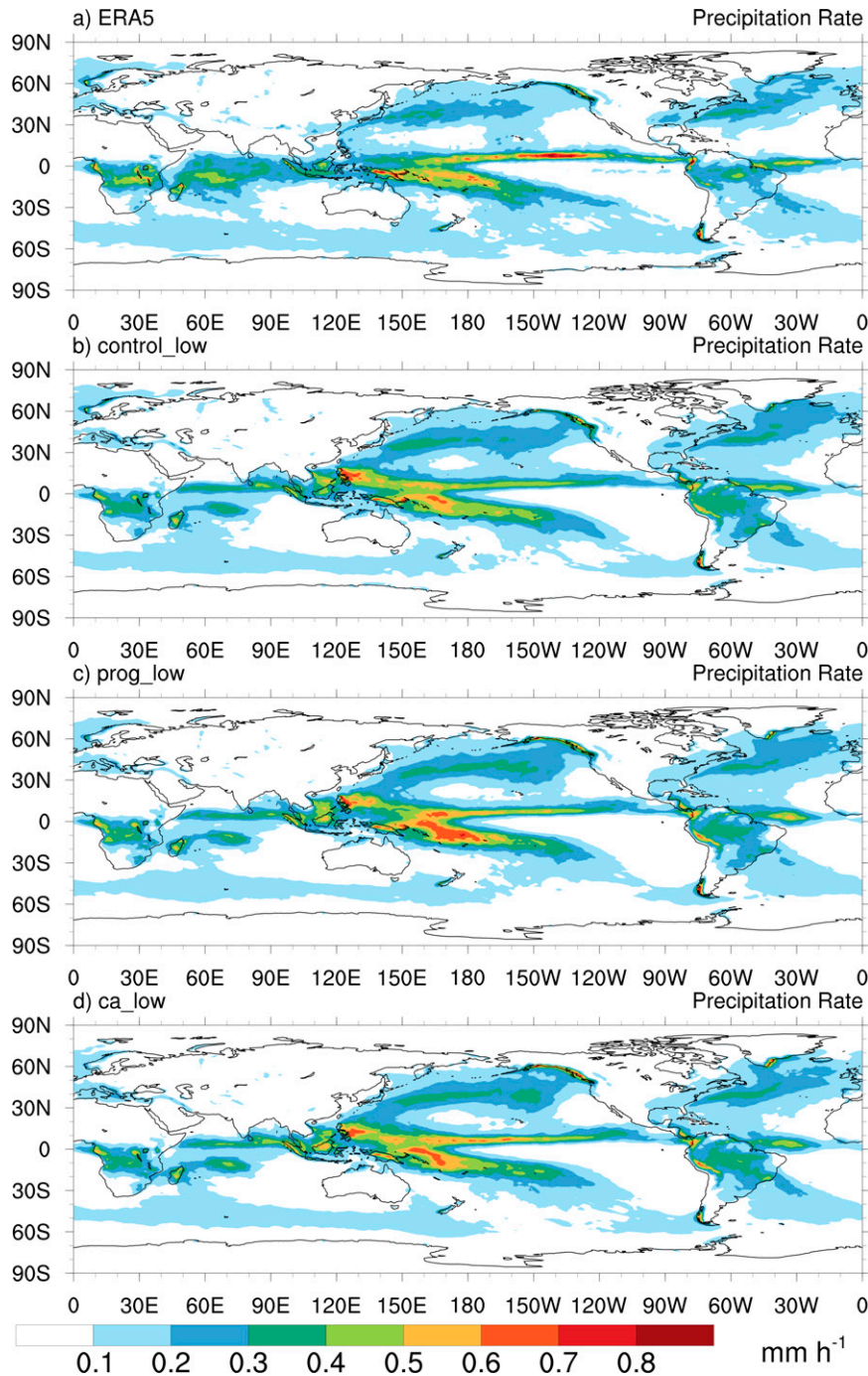


FIG. 2. Precipitation rate ( $\text{mm h}^{-1}$ ) averaged over the five different seasonal simulations over the 90-day forecast period: (a) ERA5, (b) control\_low, (c) prog\_low, and (d) ca\_low.

from the control forecast GFSv16, and the forecast with the new prognostic closure (prog\_low), and the experiment with cellular automata (ca\_low), respectively, all initialized on 29 October 2019. These diagrams show that both model runs quickly deviate from the reanalysis precipitation field, and after two weeks, it is difficult to say if one model run is performing better than the other. It can, however, be seen that the

model run with the new prognostic closure tends to generate more small-scale features, which appear to be less streaky and more organized. There is also more convection over the Indian Ocean propagating into the western Pacific Ocean in the prognostic closure experiment relative to the control run. The prog\_low and ca\_low experiments start off similarly, which is expected as the cellular automata provides a rather

TABLE 2. Total and convective global and tropical mean precipitation ( $\text{mm day}^{-1}$ ) for the three model runs control, prog\_low, and ca\_low averaged over the five initial conditions listed in Table 1.

	Control (global)	Control (tropical)	Prog_low (global)	Prog_low (tropical)	CA_low (global)	CA_low (tropical)
Total	3.05	5.19	3.07	5.29	3.05	5.35
Convective	1.82	4.46	1.78	4.50	1.79	4.54

small forcing. At longer lead times the two runs start to deviate from each other, and it appears that the ca\_low experiment has somewhat more eastward propagating features than both the control and prog\_low runs. To investigate whether there is a systematic impact on eastward- versus westward-propagating features between the different experiments, the space–time coherence spectra are investigated next.

To investigate whether the organized precipitating envelopes seen in the Hovmöller diagram are realistic, even though they might not be occurring at the correct location or time, we analyze the space–time coherence spectra between precipitation and low-level (900 hPa) moisture convergence. We follow closely the methodology outlined in Dias et al. (2018) and Gehne et al. (2022) to compute the coherence spectra, but instead of using the divergence field, we here compute the coherence between low-level moisture convergence and precipitation. Each 90-day seasonal simulation is divided into 26-day segments overlapping by 5 days. The longitude–time cross spectra are then computed for each segment and at each latitude from 15°S to 15°N, and finally averaged over latitude, segments and all the 90 day hindcasts. The symmetric component of the coherence-squared between ERA5 precipitation and 900 hPa moisture convergence (Fig. 4a) show that regions of high coherence-squared tend to match up with the Matsuno’s equatorial wave dispersion curves (Matsuno 1966) for equatorial Rossby waves, inertia–gravity waves, and Kelvin waves. Figure 4b indicates that the

GFSv16 control run overall underrepresents the observed strength of the coupling between precipitation and low-level moisture convergence and it does not display the 5-day peak associated with Kelvin waves seen in Fig. 4a. To some extent by design, Fig. 4c shows that the new prognostic closure improves the overall coupling between precipitation and low-level moisture convergence. In addition, the coherence spectra in Fig. 4c displays the Kelvin wave 5-day peak that is absent in the control case, as well as increased coherence along the spectral region associated with tropical depressions (Wheeler and Kiladis 1999). Notice that this improvement is consistent with our qualitative assessment of the Hovmöller diagrams from Fig. 3. It is interesting to note that, while there is no large systematic shift between resolved and convective precipitation, there is a systematic response in the space–time coherence spectra between low-level moisture convergence and precipitation using the cellular automata (Fig. 4d). It is difficult to assess how much of this systematic response is due to the noise induced forcing, as pointed out by Berner et al. (2018) injection of noise can have a systematic influence on oscillating systems, or how much is due to the systematic forcing of the cellular automata. The convective area fraction does increase in areas where organization is large, and this organization is conditioned on subgrid rain evaporation, which, with physical reasoning, could explain in part, the enhanced coherence between low-level moisture convergence and precipitation.

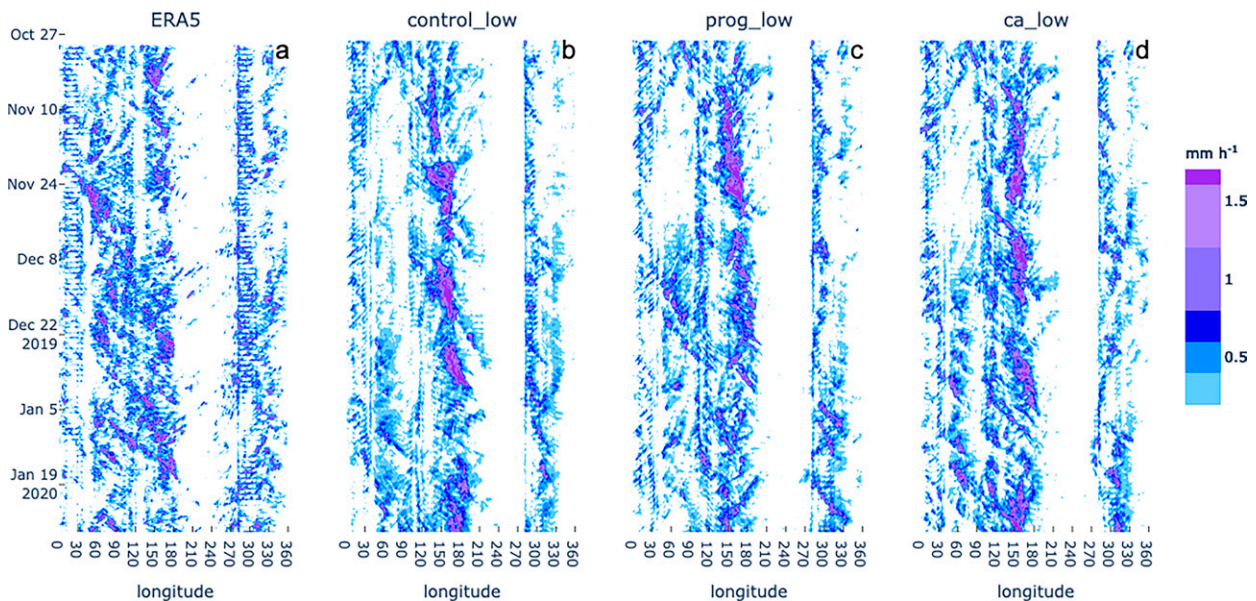


FIG. 3. Hovmöller diagram of 6-hourly precipitation ( $\text{mm h}^{-1}$ ) initialized at 29 Oct 2019 for (a) ERA5, (b) control\_low, (c) prog\_low, and (d) ca\_low. The precipitation is averaged over the latitude bands 5°S–5°N.

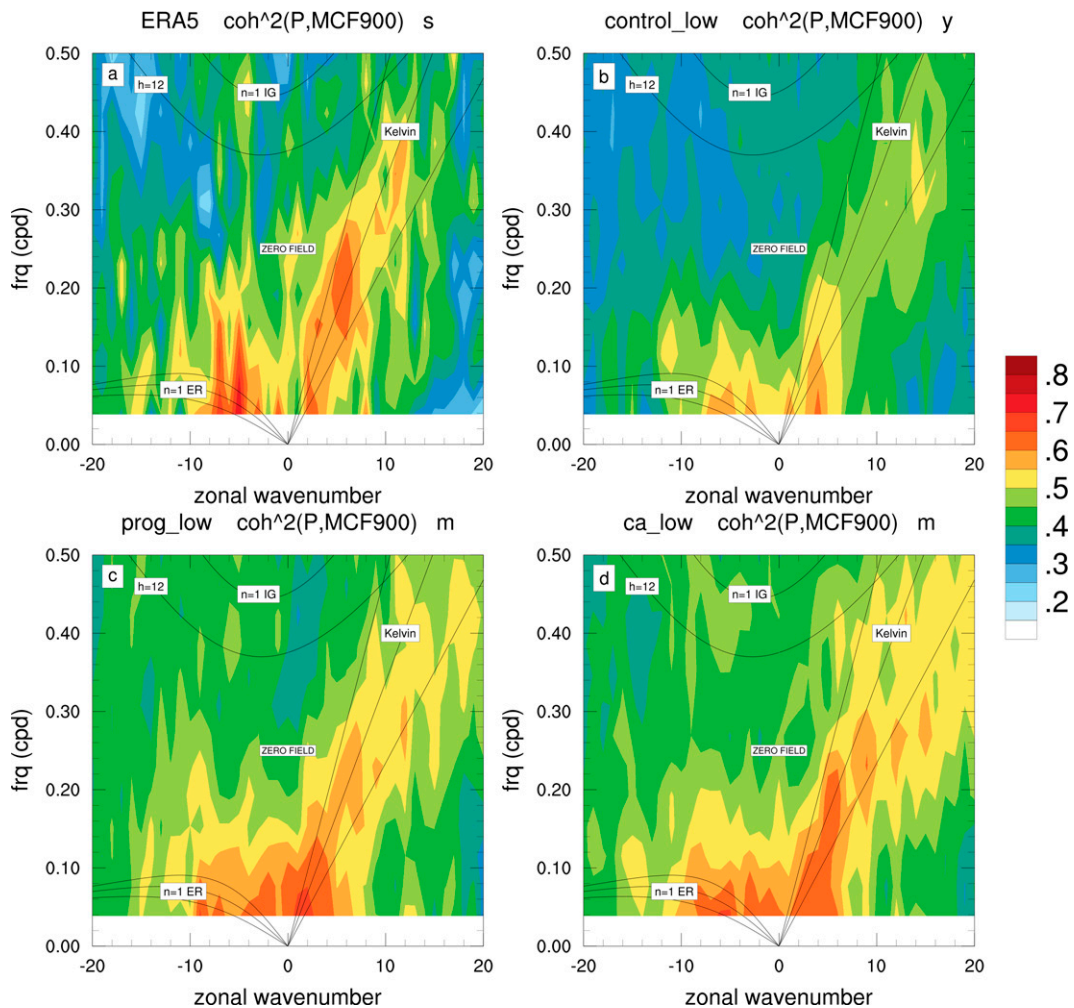


FIG. 4. Frequency in cycles per day [freq(cpd)]—zonal wavenumber coherence-squared spectra averaged over all of the seasonal simulations (90 days) from 15°S to 15°N between 900-hPa moisture flux convergence and precipitation for (a) ERA5 valid at the same dates as the 90-day forecasts (see the text for details), (c) prog\_low, and (d) ca\_low. The dispersion curves shown are for equatorial waves as in [Wheeler and Kiladis \(1999\)](#), for equivalent depths of 12, 25, and 50 m.

The results shown in [Figs. 3 and 4](#) suggest that the space–time organization and propagation of convectively coupled equatorial waves is more impacted by the updates in the cumulus convection scheme, than what the mean state is. This is an important remark as it implies that the enhancement of convective organization on the scales of equatorial waves, seen with the new prognostic closure, is not necessarily due to changes in the mean state in which the propagating wave envelopes are embedded within.

#### *b. An MJO case study: Sensitivity to closure and subgrid organization effects*

Moisture sensitivity in the cumulus convection parameterizations has shown to improve the prediction of the MJO (e.g., [Maloney and Hartmann 2001](#); [Benedict and Randall 2009](#); [Tulich and Mapes 2010](#); [Hannah and Maloney 2011](#); [Kim et al. 2012](#)). Given that our results thus far show a larger

coherence between convective precipitation and low-level moisture flux convergence using the new prognostic closure, an MJO case study is analyzed next.

For the MJO case study analysis, we carry out higher-resolution simulations using the resolution of the operational GFSv16 (13 km). The hindcasts are initialized on 19 October 2019 and the forecast goes out 26 days. The MJO amplitude and phase bias, as well as the MJO propagation phase diagram are computed following closely the methodology outlined in [Wheeler and Hendon \(2004\)](#), [Rashid et al. \(2011\)](#) and [Kim et al. \(2018\)](#), which uses projected data onto the leading empirical orthogonal functions (EOFs). The principal component time series forms an index called the Real-Time Multivariate MJO series 1 (RMM1) and 2 (RMM2) ([Wheeler and Hendon 2004](#)). The forecasts are analyzed in terms of projections of the forecasted meridional wind component at 200 and 850 hPa as well as the outgoing longwave radiation (OLR) onto the RMM indices as

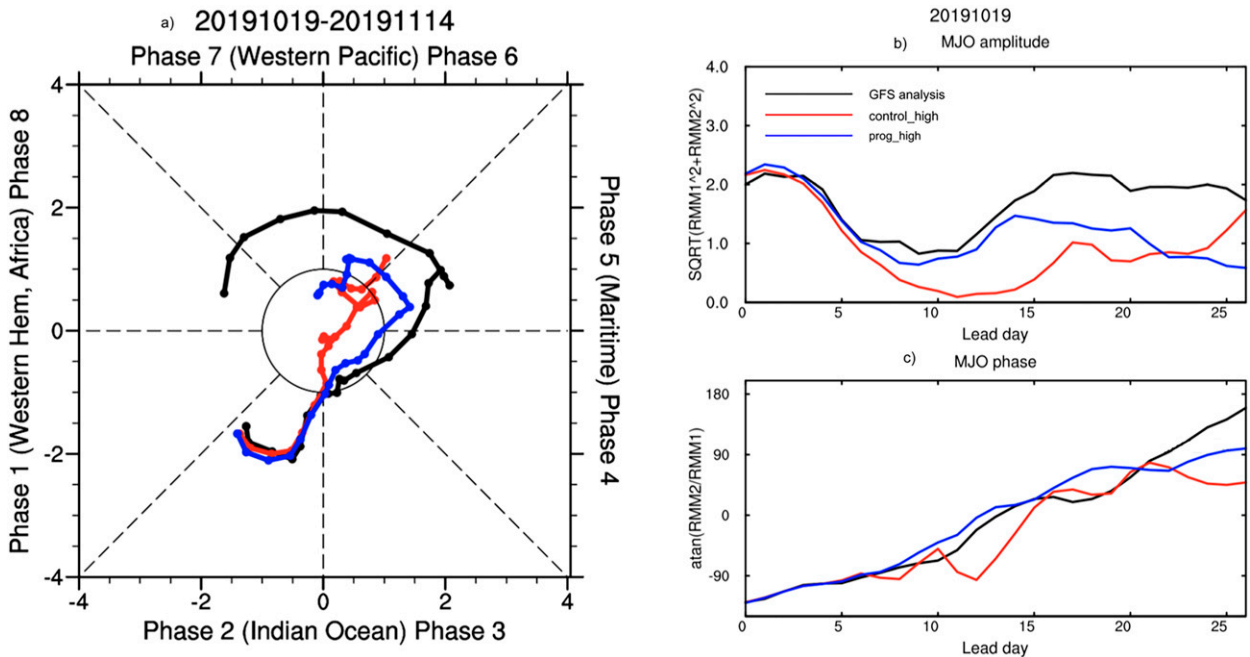


FIG. 5. (a) MJO phase diagram, (b) MJO amplitude bias, and (c) MJO phase bias (arctangent of  $\text{RMM2}/\text{RMM1}$ ) for the GFS analysis (black), control\_high (red), and prog\_high (blue). The MJO phase diagram is calculated as in Kim et al. (2018) and Rashid et al. (2011).

displayed in the two-dimensional phase-space (Fig. 5a), and amplitude and phase errors can be computed by treating the RMM indices as a bivariate index following closely Eqs. (1)–(4) in Rashid et al. (2011) (Figs. 5b,c).

Figure 5 shows the MJO amplitude, phase, and propagation for the GFS analysis (Kleist et al. 2009) in black, the control GFSv16 in red, and the experimental run with the new prognostic closure in blue. It can be seen that the experiments with the prognostic closure lead to an improvement in both phase and amplitude as well as propagation. While the MJO in the control run tends to stagnate over the western Pacific, the MJO in the hindcast with the prognostic closure appears to follow the analysis closer for about one additional week in comparison with control. The amplitude is higher in the hindcast with the prognostic closure, and nicely picks up in amplitude when the analysis picks up at around day 12. The phase-speed is increased in the experiment run and matches better with the analysis when compared with the control run. Taken together with the previous analysis, it appears that the enhanced relationship between low-level moisture convergence and convective precipitation can be beneficial for prediction of the MJO in the GFS as demonstrated by this case study. More cases would need to be explored to understand whether this is a systematic impact of the new closure description on different MJO events.

We next explore the impact of the stochastic cellular automaton. In these simulations, the prognostic area fraction is further enhanced in regions where a stochastic self-organizing cellular automaton has formed sufficiently large clusters on the subgrid. The cellular automaton follows closely the methodology outlined in Bengtsson et al. (2021), and is conditioned on subgrid

rain evaporation—thus it becomes more organized in regions related to strong evaporation/cooling from falling convective precipitation. Figure 6 shows the same analysis as presented in Fig. 5, with the addition of five runs with the prognostic closure plus a stochastic enhancement of the area fraction from the cellular automaton (gray curves). The cellular automata simulations differ by having a different stochastic seed in its initialization.

A couple of conclusions can be drawn; first, it appears that the runs with the stochastic parameterizations do not start to diverge until after about one week into the simulation, suggesting that the signal from the initial state is dominating the predictability at these early lead times. After about one week, the forecasts diverge as the stochastic convection has modulated the large-scale flow in different directions, which can be interpreted as a noise induced forcing. In terms of propagation and amplitude, the GFS analysis is centered among the different perturbed ensemble members initially, however, at longer lead times the amplitude of the MJO seems to systematically be increased in the runs using cellular automata. Another observation is that the ensemble spread among the members is larger for the MJO amplitude than it is for the MJO phase. There also seems to be a systematic impact in that the enhanced organization provided by the cellular automaton tends to increase the amplitude of the MJO at longer lead times, but at the same time also systematically slows down the MJO phase speed. The increase in amplitude and decrease in phase speed is consistent with the impact of the cellular automaton in reducing the so-called effective normalized gross moist stability that is shown in Bengtsson et al. (2021). The effective normalized gross moist stability is an important

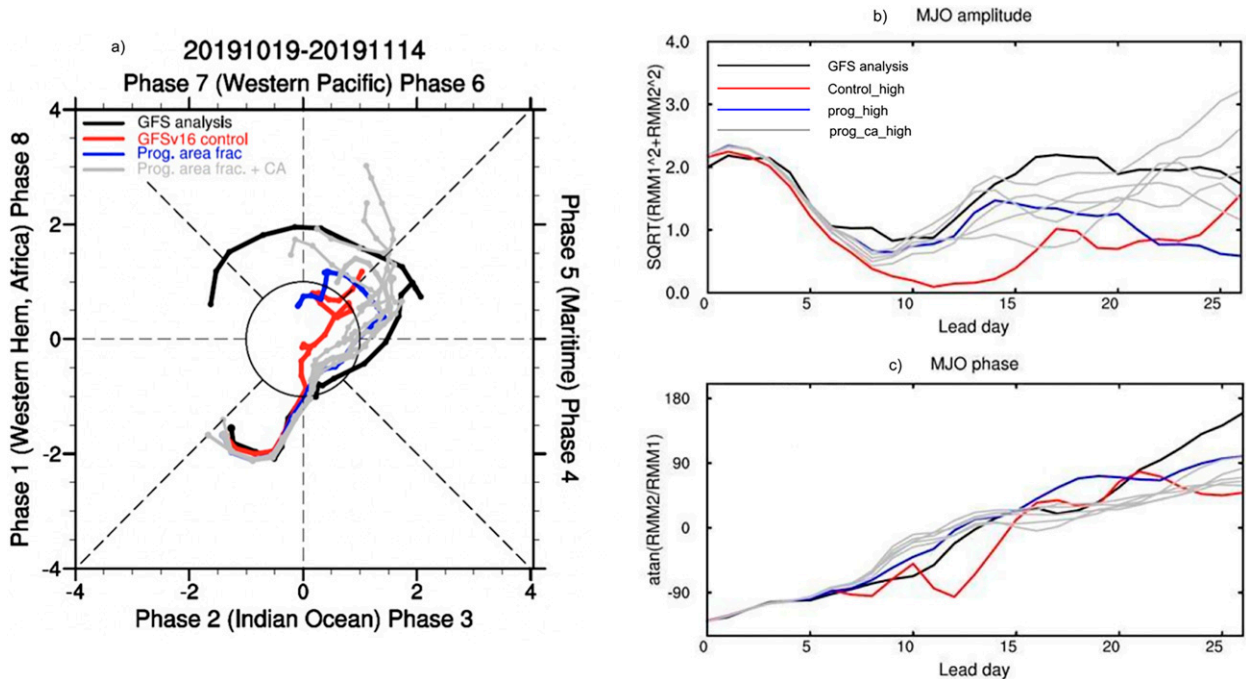


FIG. 6. As in Fig. 6, but with five members of prog\_ca\_high (gray) added to the plots.

quantity in the study of tropical moisture modes (e.g., [Adames and Maloney 2021](#), and references therein) because it diagnoses the impact of convection on the thermodynamic environment due to moisture–convection and cloud–radiation feedbacks, which, in turn, affect the MJO propagation and maintenance. In a future study we plan on evaluating how the new closure fully impacts these feedbacks and therefore simulations of the MJO. The cellular automata results suggest that while there could be some room for improvement in terms of the impact on MJO phase speed, the methodology offers a novel approach to parameterizing a feedback from subgrid convective organization, and offers a methodology to provide uncertainty estimates associated with cumulus convection on seasonal prediction.

### c. Scale-adaptive behavior of the scheme

As stated previously, the expectation is that the convective area fraction should increase with decreasing grid size, as a larger fraction of the grid box will be taken up by cumulus convection. At the same time, with decreasing gridbox length, more mesoscale motion will be resolved by the model dynamics, and the parameterized mass flux should thus decrease with decreasing grid size, to allow the model to resolve more vertical motions associated with convection. Thus, the global simulations using 3-km grid spacing are expected to have a reduction of subgrid convective precipitation, which is taken over by the model-resolved precipitation.

The first question to consider is if we can expect that the prognostic updraft area fraction, as given by Eq. (8), will approach 1 with decreasing grid size? To answer that, there are several factors to consider. First, discretizing Eq. (8) and

solving for  $\sigma_B$ , where the next time step is indicated by a superscript plus sign and the previous time step is indicated by a superscript minus sign, in the first term on the rhs of Eq. (8) gives

$$\sigma_B^+ = \frac{A + D}{B + C}, \quad (12)$$

where

$$A = \sum_{l=1}^L f^l [\xi^l (h_u - h_s)]^l \Delta p^l \sigma_B^-,$$

$$B = \sum_{l=1}^L f^l [\xi^l (h_u - h_s)]^l \Delta p^l,$$

$$C = \sum_{l=1}^L f^l L^l (-\omega_u \Delta t \delta q_{\text{cond}} \xi)^l \Delta p^l, \quad \text{and}$$

$$D = \sum_{l=1}^L f^l L^l \text{MFC}^l \Delta p^l,$$

where  $l$  represents model levels,  $f^l$  is an integer that takes on the value 1.0 if the model level is positively buoyant and has integrated (from the surface to current level) positive moisture flux convergence; otherwise, it is 0.0. The other terms are as explained after Eq. (8). From Eq. (12) it can be seen that the size of the area fraction is primarily determined by the ratio between the source term  $D$  (moisture flux convergence), and the sink term  $C$  (moisture converted into cloud in the updraft). Term  $C$  (in the denominator) does decrease with decreasing grid size because of the updraft vertical velocity in term  $C$  decreases with decreasing grid size, whereas term  $D$  is

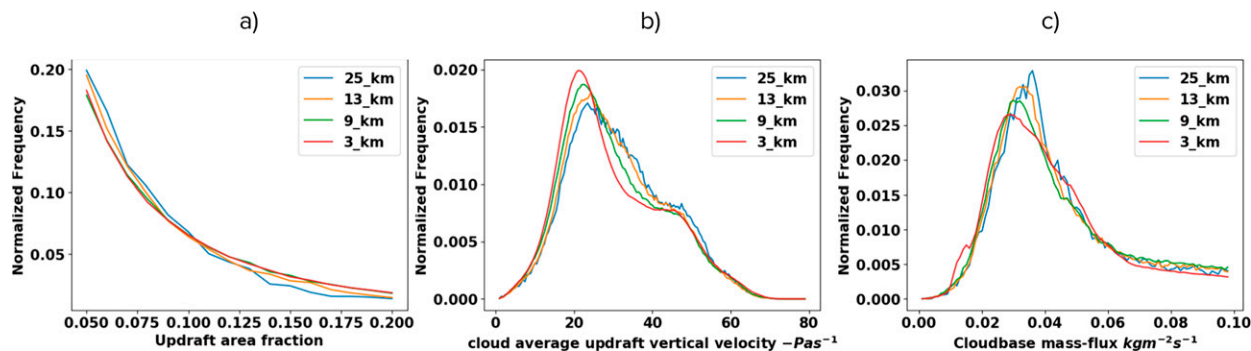


FIG. 7. Normalized frequency distribution of (a) updraft area fraction (%), (b) cloud average updraft velocity ( $-\text{Pa s}^{-1}$ ), where values are multiplied by  $-1.0$  such that larger positive values are associated with stronger updrafts, and (c) cloud base mass-flux ( $\text{kg m}^{-2} \text{s}^{-1}$ ). Blue, orange, green, and red curves are fields extracted from the prog\_25\_short, prog\_13\_short, prog\_9\_short, and prog\_3\_short experiments, respectively.

generally similar across the different resolutions (not shown). This behavior thus leads to an increase in updraft area fraction with decreasing grid size. However, since the terms in Eq. (12) are vertical integrals over buoyant levels with positive moisture flux convergence accumulated from the surface, the number of vertical levels integrated over are significantly fewer in the 3-km simulation, relative to the other resolutions. Thus, it is not straightforward to conclude from Eq. (12) alone that the updraft area fraction will be much larger at 3 km than in the 25-km run because the ratio between the terms needs to be considered.

Figure 7 shows the normalized frequency distribution of the updraft area fraction, the cloud average updraft velocity and the cloud-base mass flux from the deep cumulus convection scheme from our experiment simulation. The values shown are the instantaneous values after a 24-h forecast, on the native grids of the different resolution simulations. The majority of the updraft area fraction values are smaller than 0.1, and we here zoom in on the values between 0.05 and 0.2. The distribution of the updraft area fraction generally does shift with decreasing gridbox size, showing somewhat increased area fractions with decreasing gridbox size. The 3- and 9-km distributions are quite similar; one explanation for this can be attributed to the change in number of active levels in the 3-km simulation as explained above. Furthermore, importantly, the gridbox size is not the only factor impacting the updraft area fraction value, as it is also determined based on the moisture budget equation source and sink terms. Figure 7b shows the distribution of the cloud average updraft velocity ( $\text{Pa s}^{-1}$ , here multiplied by  $-1$ , such that large positive values indicate strong updrafts). The peak of the distribution is clearly shifted as a function of decreasing grid size, illustrating that the updraft velocity is reduced when the buoyancy in the grid box is reduced. This stems from the fact that the buoyancy term in Eq. (5) is computed as the difference between the updraft and grid average properties. Thus, given the same size of the area consumed by convection, a smaller grid box would lead to mean gridbox values (the mean of the updraft and environment properties) that are closer to the updraft properties. Therefore, computing the buoyancy using the difference between updraft and mean

gridbox values yields a smaller buoyancy with decreasing gridbox size, and consequently a reduced updraft vertical velocity. Similarly, the peak of the distribution of the cloud-base mass flux (Fig. 7c) is also reduced with decreasing grid spacing, and the distribution tail values (larger mass fluxes) are reduced in the 3-km simulation. We thus conclude that the proposed formulation of the cloud-base mass flux is scale adaptive, as the mass flux is reduced with decreasing gridbox size, and as noted, the main reason for this scale adaptiveness is due to the updraft velocity being reduced with decreasing grid spacing, and only partly due to the change in area fraction with decreasing gridbox size.

The partitioning between subgrid convective and resolved precipitation at different resolutions is investigated next. The resolved and subgrid convective precipitation partitioning at 25, 13, 9, and 3 km are considered in the control GFSv16 forecast as well as in the experiment with the prognostic area fraction, and are presented in Table 3 for the tropical band  $10^{\circ}\text{S}$ – $10^{\circ}\text{N}$ , as well as over the global domain. The precipitation values for all the experiment presented in Table 3 are first coarse grained to a common 25-km-resolution grid.

Observations and reanalysis indicate that the climatology of the global mean total precipitation is around  $2.7$ – $3.3 \text{ mm day}^{-1}$  (Hassler and Lauer 2021). For instance, the Global Precipitation Climatology Project (GPCP) states that the estimated mean global precipitation for 2020 from their monthly analysis is  $2.70 \text{ mm day}^{-1}$ , almost exactly the 40-yr climatological mean of  $2.69$  (Adler et al. 2003), whereas NCEP reanalysis monthly precipitation data over the past 30 years from 1979 to 2008 show a global mean around  $3.1 \text{ mm day}^{-1}$  (Li et al. 2015). Thus, this precipitation range is often used as a benchmark when developing global numerical weather prediction models. Table 3 shows that the global mean total precipitation in the control simulation is around  $2.9 \text{ mm day}^{-1}$  for the 25- and 13-km resolution; however, the precipitation forecast does not scale well, and the total precipitation at the higher resolutions (9 and 3 km) underestimates the mean total precipitation (around  $2.5 \text{ mm day}^{-1}$ ). As expected, at the higher resolutions the precipitation contribution from the subgrid convection scheme is scaled down, however, in the control GFSv16

TABLE 3. Total and convective global and tropical mean precipitation ( $\text{mm day}^{-1}$ ), computed at forecast lead time 24 h for the control and prognostic closure simulations at 25-, 13-, 9-, and 3-km resolution, coarse grained to a common 25-km grid before taking the latitude weighted mean.

	Global mean total precipitation	Global mean convective precipitation	Tropical mean total precipitation	Tropical mean convective precipitation
Control_25_short	2.91	1.88	5.38	4.58
Prog_25_short	2.96	1.86	5.79	4.82
Control_13_short	2.92	1.81	5.40	4.52
Prog_13_short	2.97	1.81	5.69	4.65
Control_9_short	2.53	0.85	4.57	2.11
Prog_9_short	3.01	1.86	5.59	4.60
Control_3_short	2.48	0.45	4.35	1.07
Prog_3_short	2.82	0.85	5.29	2.07

simulation a large reduction in convective precipitation over the tropics, specifically over the central Pacific and south America (not shown) is not compensated for by resolved convection. One reason for this could be that, while the subgrid mass-flux scheme is scaled down, there is still enough subgrid convection acting to stabilize the atmosphere inhibiting convection to be initiated over the tropical ocean. The prognostic closure experiment has somewhat larger values of total precipitation in the global mean (around  $3.0 \text{ mm day}^{-1}$ ), but does scale better across the resolutions than the control, mainly as a consequence of maintaining more subgrid convection at the higher resolutions over the tropics [in particular over the central Pacific (not shown)]. Because of the exceptionally high computational cost of the global 3-km simulations, it was not possible to generate longer simulations to investigate the scale-adaptive behavior at longer lead times, it should be noted that the spinup of model variables to reach an equilibrium state can impact these results.

## 6. Conclusions and future outlook

In this study we implemented and evaluated the impact of a prognostic-stochastic closure in the Global Forecast System application of NOAA's Unified Forecast System. The closure is based on a moisture budget (in addition to the buoyancy driven updraft velocity term) providing a prognostic evolution of the convective updraft area fraction. The impact of the new prognostic closure is evaluated in terms of large-scale moisture coupling to convection, its impact on tropical variability, and the precipitation mean state. In addition, we study the scheme's ability to adapt across various gridbox sizes as the updraft area fraction is also a function of the grid box itself. The following points represent our main findings:

- While the precipitation mean state is not largely influenced by the updates to the convection scheme, the space–time organization of convectively coupled equatorial waves is. We find that model simulations including the new prognostic closure enhance the coherence between low-level moisture convergence and rainfall associated with the MJO, and convectively coupled equatorial waves, suggesting that there is a tighter coupling between dynamics, low-level moisture and parameterized cumulus convection. The enhanced coherence between low-level moisture convergence and precipitation

with the proposed parameterization is closer to the observed coherence seen in the ERA5 reanalysis dataset. The Hovmöller diagram also shows more small-scale features and activity in the Indian Ocean propagating convective wave envelopes into the western Pacific.

- The amplitude, phase, and propagation of a case study MJO event with the new prognostic closure is improved, when compared with the control GFSv16 simulation, better agreeing with the GFS analysis. Given the large number of studies in the literature suggesting that the MJO representation is improved when the convection is made more sensitive to tropospheric moisture, our results indicate that, at least in part, the improvements that we find in the MJO event can be attributed to the closer coherence between low-level moisture flux convergence and precipitation along these wave modes. More MJO cases need to be studied in order to fully understand the systematic impact of the newly proposed closure on the MJO.
- Inclusion of enhanced organization feedback and stochasticity in the cumulus convection as modeled by self-organizing cellular automata suggests that the MJO propagation and amplitude is sensitive to small perturbations within the convection scheme, and the propagation tracks start to diverge after about 2 weeks (far away from the initial state). Toward the end of the simulation (after three weeks), the impact of the cellular automata appears to be a systematic enhancement in MJO amplitude, and a systematic reduction in MJO phase speed. The ensemble spread is centered around the GFS analysis, suggesting that the uncertainty estimates provided by such noise induced forcing are reliable.
- Last, we study the scale-adaptive behavior of the new prognostic closure. We find that, at 3-km grid spacing, the convective precipitation is reduced less in our experiment simulation, than the convective precipitation in the GFSv16 control simulation. However, it appears that the resolved precipitation does not pick up sufficiently over the central Pacific in the control run, and thus, in this particular region the convection does not scale well across resolutions in the control. We also conclude that the scale-adaptive behavior of the scheme is mainly attributable to a large decrease in parameterized updraft velocity with decreasing grid size. The scale adaptiveness of the updraft area fraction itself is complex as the physical quantities in the prognostic

equation are integrated over buoyant layers, which themselves change drastically depending on gridbox size.

This study is in agreement with previous literature indicating that the quasi-equilibrium steady state assumption in cumulus parameterizations becomes invalid as the gridbox size decreases, since the assumption of negligible area fraction is no longer applicable and, to address this limitation, we proposed an alternative cumulus convection closure for use in NOAA's Unified Forecast System. It also confirms the findings in previous studies that have demonstrated that convectively coupled equatorial waves are highly sensitive to the cumulus convection scheme in NWP models, and that a closer coupling between low-level moisture and cumulus convection is important for MJO prediction. Therefore, improvement of NOAA's Unified Forecast System performance in the tropics, and the downstream effect on the global scale of such improvement, can benefit from the proposed updates to the convection scheme outlined in this study.

In this study we did not carry out an evaluation of the scheme's performance in terms of precipitation prediction skill. We anticipate that seeing any statistically significant improvement in terms of such skill metrics will require careful integration with other physics components such as PBL and microphysics schemes and optimization of the model performance via careful calibration of the whole physics suite. Our near term plan is to move forward with such a physics suite integration based on the latest version of the UFS model code base, which has seen substantial updates in the model physics, relative to the current operation version GFSv16. In addition, we further aim to evaluate the scheme's performance in terms of tropical cyclones because their track and intensity are highly sensitive to the strength of the mass flux in the cumulus convection scheme.

*Acknowledgments.* The authors thank the two reviewers of this paper for their careful and insightful revisions. The authors also thank Dr. Brandon Wolding, CIRES/NOAA PSL, for a careful internal (NOAA PSL) review of the paper. The authors also acknowledge the valuable discussions held within the UFS convection working group, which have contributed to improving the research presented in this study. The research was partially funded by four sources: 1) the NOAA/ESRL/Physical Science Laboratory (PSL), 2) the California Department of Water Resources (CDWR), 3) the NOAA/UFS Research to Operations (UFSR2O) project, and 4) Further Additional Supplemental Appropriations (IFAA) for Disaster Relief Requirements Act, 2018, Pub. L. 115-123, div. B, subdiv. 1, Feb. 9, 2018, 132 Stat. 65, 70. The Act allocated to NOAA \$50 million to improve weather forecasting, hurricane intensity forecasting, and flood forecasting and mitigation capabilities, including data assimilation from ocean observing platforms and satellites.

*Data availability statement.* The model output for the reference and cellular automata configurations used in this study can be accessed online ([https://downloads.psl.noaa.gov/Projects/FAIR\\_paper\\_data/20220422\\_01/](https://downloads.psl.noaa.gov/Projects/FAIR_paper_data/20220422_01/)), as can the ERA5 data (<https://www.ecmwf.int/en/forecasts/dataset/ecmwf-reanalysis-v5>).

## REFERENCES

- Adames, Á. F., and E. D. Maloney, 2021: Moisture mode theory's contribution to advances in our understanding of the Madden-Julian Oscillation and other tropical disturbances. *Curr. Climate Change Rep.*, **7**, 72–85, <https://doi.org/10.1007/s40641-021-00172-4>.
- Adler, R. F., and Coauthors, 2003: The version-2 Global Precipitation Climatology Project (GPCP) Monthly Precipitation Analysis (1979–present). *J. Hydrometeor.*, **4**, 1147–1167, [https://doi.org/10.1175/1525-7541\(2003\)004<1147:TVGPCP>2.0.CO;2](https://doi.org/10.1175/1525-7541(2003)004<1147:TVGPCP>2.0.CO;2).
- Arakawa, A., and W. H. Schubert, 1974: Interaction of a cumulus cloud ensemble with the large-scale environment. Part I. *J. Atmos. Sci.*, **31**, 674–701, [https://doi.org/10.1175/1520-0469\(1974\)031<0674:IOACCE>2.0.CO;2](https://doi.org/10.1175/1520-0469(1974)031<0674:IOACCE>2.0.CO;2).
- , and C. Wu, 2013: A unified representation of deep moist convection in numerical modeling of the atmosphere. Part I. *J. Atmos. Sci.*, **70**, 1977–1992, <https://doi.org/10.1175/JAS-D-12-0330.1>.
- Bechtold, P., N. Semane, P. Lopez, J.-P. Chaboureaud, A. Beljaars, and N. Bormann, 2014: Representing equilibrium and non-equilibrium convection in large-scale models. *J. Atmos. Sci.*, **71**, 734–753, <https://doi.org/10.1175/JAS-D-13-0163.1>.
- Benedict, J. J., and D. A. Randall, 2009: Structure of the Madden-Julian oscillation in the superparameterized CAM. *J. Atmos. Sci.*, **66**, 3277–3296, <https://doi.org/10.1175/2009JAS3030.1>.
- Bengtsson, L., M. Steinheimer, P. Bechtold, and J.-F. Geleyn, 2013: A stochastic parameterization for deep convection using cellular automata. *Quart. J. Roy. Meteor. Soc.*, **139**, 1533–1543, <https://doi.org/10.1002/qj.2108>.
- , J. Bao, P. Pegion, C. Penland, S. Michelson, and J. Whitaker, 2019a: A model framework for stochastic representation of uncertainties associated with physical processes in NOAA's Next Generation Global Prediction System (NGGPS). *Mon. Wea. Rev.*, **147**, 893–911, <https://doi.org/10.1175/MWR-D-18-0238.1>.
- , and Coauthors, 2019b: Convectively coupled equatorial wave simulations using the ECMWF IFS and the NOAA GFS cumulus convection schemes in the NOAA GFS model. *Mon. Wea. Rev.*, **147**, 4005–4025, <https://doi.org/10.1175/MWR-D-19-0195.1>.
- , J. Dias, S. Tulich, M. Gehne, and J.-W. Bao, 2021: A stochastic parameterization of organized tropical convection using cellular automata for global forecasts in NOAA's Unified Forecast System. *J. Adv. Model. Earth Syst.*, **13**, e2020MS002260, <https://doi.org/10.1029/2020MS002260>.
- Berner, J., P. D. Sardeshmukh, and H. M. Christensen, 2018: On the dynamical mechanisms governing El Niño–Southern Oscillation irregularity. *J. Climate*, **31**, 8401–8419, <https://doi.org/10.1175/JCLI-D-18-0243.1>.
- Chen, J.-H., and S.-J. Lin, 2013: Seasonal predictions of tropical cyclones using a 25-km-resolution general circulation model. *J. Climate*, **26**, 380–398, <https://doi.org/10.1175/JCLI-D-12-00061.1>.
- Chen, X., L. R. Leung, Z. Feng, and Q. Yang, 2022: Precipitation-moisture coupling over tropical oceans: Sequential roles of shallow, deep, and mesoscale convective systems. *Geophys. Res. Lett.*, **49**, e2022GL097836, <https://doi.org/10.1029/2022GL097836>.
- Chikira, M., and M. Sugiyama, 2010: A cumulus parameterization with state-dependent entrainment rate. Part I: Description and sensitivity to temperature and humidity profiles. *J. Atmos. Sci.*, **67**, 2171–2193, <https://doi.org/10.1175/2010JAS3316.1>.
- Chopard, B., and M. Droz, 1998: *Cellular Automata Modeling of Physical Systems*. Cambridge University Press, <https://doi.org/10.1017/CBO9780511549755>.

- Davies, L., C. Jakob, P. May, V. V. Kumar, and S. Xie, 2013: Relationships between the large-scale atmosphere and the small-scale convective state for Darwin, Australia. *J. Geophys. Res. Atmos.*, **118**, 11 534–11 545, <https://doi.org/10.1002/jgrd.50645>.
- Dias, J., M. Gehne, G. N. Kiladis, N. Sakaeda, P. Bechtold, and T. Haiden, 2018: Equatorial waves and the skill of NCEP and ECMWF numerical weather prediction systems. *Mon. Wea. Rev.*, **146**, 1763–1784, <https://doi.org/10.1175/MWR-D-17-0362.1>.
- , S. N. Tulich, M. Gehne, and G. N. Kiladis, 2021: Tropical origins of weeks 2–4 forecast errors during the Northern Hemisphere cool season. *Mon. Wea. Rev.*, **149**, 2975–2991, <https://doi.org/10.1175/MWR-D-21-0020.1>.
- Dorrestijn, J., D. T. Crommelin, A. P. Siebesma, and H. J. J. Jonker, 2013: Stochastic parameterization of shallow cumulus convection estimated from high-resolution model data. *Theor. Comput. Fluid Dyn.*, **27**, 133–148, <https://doi.org/10.1007/s00162-012-0281-y>.
- , —, —, —, and C. Jakob, 2015: Stochastic parameterization of convective area fractions with a multicloud model inferred from observational data. *J. Atmos. Sci.*, **72**, 854–869, <https://doi.org/10.1175/JAS-D-14-0110.1>.
- Feng, Z., and Coauthors, 2021: A global high-resolution mesoscale convective system database using satellite-derived cloud tops, surface precipitation, and tracking. *J. Geophys. Res. Atmos.*, **126**, e2020JD034202, <https://doi.org/10.1029/2020JD034202>.
- Frenkel, Y., A. J. Majda, and B. Khouider, 2013: Stochastic and deterministic multicloud parameterizations for tropical convection. *Climate Dyn.*, **41**, 1527–1551, <https://doi.org/10.1007/s00382-013-1678-z>.
- Gehne, M., B. Wolding, J. Dias, and G. Kiladis, 2022: Diagnostics of tropical variability for numerical weather forecasts. *Wea. Forecasting*, **37**, 1661–1680, <https://doi.org/10.1175/WAF-D-21-0204.1>.
- Gerard, L., 2015: Bulk mass-flux perturbation formulation for a unified approach of deep convection at high resolution. *Mon. Wea. Rev.*, **143**, 4038–4063, <https://doi.org/10.1175/MWR-D-15-0030.1>.
- , and J.-F. Geleyn, 2005: Evolution of a subgrid deep convection parametrization in a limited area model with increasing resolution. *Quart. J. Roy. Meteor. Soc.*, **131**, 2293–2312, <https://doi.org/10.1256/qj.04.72>.
- , J.-M. Piriou, R. Brožková, J.-F. Geleyn, and D. Banciu, 2009: Cloud and precipitation parameterization in a meso-gamma scale operational weather prediction model. *Mon. Wea. Rev.*, **137**, 3960–3977, <https://doi.org/10.1175/2009MWR2750.1>.
- Gottwald, G. A., K. Peters, and L. Davies, 2016: A data-driven method for the stochastic parameterisation of subgrid-scale tropical convective area fraction. *Quart. J. Roy. Meteor. Soc.*, **142**, 349–359, <https://doi.org/10.1002/qj.2655>.
- Grell, G. A., 1993: Prognostic evaluation of assumptions used by cumulus parameterizations. *Mon. Wea. Rev.*, **121**, 764–787, [https://doi.org/10.1175/1520-0493\(1993\)121<0764:PEOAU>2.0.CO;2](https://doi.org/10.1175/1520-0493(1993)121<0764:PEOAU>2.0.CO;2).
- , and S. R. Freitas, 2014: A scale and aerosol aware stochastic convective parameterization for weather and air quality modeling. *Atmos. Chem. Phys.*, **14**, 5233–5250, <https://doi.org/10.5194/acp-14-5233-2014>.
- Hagos, S., Z. Feng, R. S. Plant, R. A. Houze, and H. Xiao, 2018: A stochastic framework for modeling the population dynamics of convective clouds. *J. Adv. Model. Earth Syst.*, **10**, 448–465, <https://doi.org/10.1002/2017MS001214>.
- Han, J., and H. Pan, 2011: Revision of convection and vertical diffusion schemes in the NCEP Global Forecast System. *Wea. Forecasting*, **26**, 520–533, <https://doi.org/10.1175/WAF-D-10-05038.1>.
- , and C. S. Bretherton, 2019: TKE-based moist Eddy-Diffusivity Mass-Flux (EDMF) parameterization for vertical turbulent mixing. *Wea. Forecasting*, **34**, 869–886, <https://doi.org/10.1175/WAF-D-18-0146.1>.
- , W. Wang, Y. C. Kwon, S. Hong, V. Tallapragada, and F. Yang, 2017: Updates in the NCEP GFS cumulus convection schemes with scale and aerosol awareness. *Wea. Forecasting*, **32**, 2005–2017, <https://doi.org/10.1175/WAF-D-17-0046.1>.
- Hannah, W. M., and E. D. Maloney, 2011: The role of moisture–convection feedbacks in simulating the Madden–Julian oscillation. *J. Climate*, **24**, 2754–2770, <https://doi.org/10.1175/2011JCLI3803.1>.
- Harris, L. M., S. Lin, and C. Tu, 2016: High-resolution climate simulations using GFDL HiRAM with a stretched global grid. *J. Climate*, **29**, 4293–4314, <https://doi.org/10.1175/JCLI-D-15-0389.1>.
- Hassler, B., and A. Lauer, 2021: Comparison of reanalysis and observational precipitation datasets including ERA5 and WFDE5. *Atmosphere*, **12**, 1462, <https://doi.org/10.3390/atmos12111462>.
- Hersbach, H., and Coauthors, 2020: The ERA5 global reanalysis. *Quart. J. Roy. Meteor. Soc.*, **146**, 1999–2049, <https://doi.org/10.1002/qj.3803>.
- Hohenegger, C., and C. Schär, 2007: Predictability and error growth dynamics in cloud-resolving models. *J. Atmos. Sci.*, **64**, 4467–4478, <https://doi.org/10.1175/2007JAS2143.1>.
- Honnert, R., V. Masson, and F. Couvreur, 2011: A diagnostic for evaluating the representation of turbulence in atmospheric models at the kilometeric scale. *J. Atmos. Sci.*, **68**, 3112–3131, <https://doi.org/10.1175/JAS-D-11-061.1>.
- Houze, R. A., Jr., 2004: Mesoscale convective systems. *Rev. Geophys.*, **42**, RG4003, <https://doi.org/10.1029/2004RG000150>.
- Hovmöller, E., 1949: The trough-and-ridge diagram. *Tellus*, **1**, 62–66, <https://doi.org/10.3402/tellusa.v1i2.8498>.
- Huang, X.-Y., 1988: The organization of moist convection by internal gravity waves. *Tellus*, **42A**, 270–285, <https://doi.org/10.3402/tellusa.v42i2.11877>.
- Jones, C., J. Gottschalck, L. M. V. Carvalho, and W. Higgins, 2011: Influence of the Madden–Julian oscillation on forecasts of extreme precipitation in the contiguous United States. *Mon. Wea. Rev.*, **139**, 332–350, <https://doi.org/10.1175/2010MWR3512.1>.
- Judt, F., 2020: Atmospheric predictability of the tropics, middle latitudes, and polar regions explored through global storm-resolving simulations. *J. Atmos. Sci.*, **77**, 257–276, <https://doi.org/10.1175/JAS-D-19-0116.1>.
- Khouider, B., J. Biello, and A. Majda, 2010: A stochastic multicloud model for tropical convection. *Commun. Math. Sci.*, **8**, 187–216, <https://doi.org/10.4310/CMS.2010.v8.n1.a10>.
- Kiladis, G. N., M. C. Wheeler, P. T. Haertel, K. H. Straub, and P. E. Roundy, 2009: Convectively coupled equatorial waves. *Rev. Geophys.*, **47**, RG2003, <https://doi.org/10.1029/2008RG000266>.
- Kim, D., A. H. Sobel, A. D. D. Genio, Y. Chen, S. J. Camargo, M.-S. Yao, M. Kelley, and L. Nazarenko, 2012: The tropical subseasonal variability simulated in the NASA GISS general circulation model. *J. Climate*, **25**, 4641–4659, <https://doi.org/10.1175/JCLI-D-11-00447.1>.
- Kim, H., F. Vitart, and D. E. Waliser, 2018: Prediction of the Madden–Julian oscillation: A review. *J. Climate*, **31**, 9425–9443, <https://doi.org/10.1175/JCLI-D-18-0210.1>.

- Kleist, D. T., D. F. Parrish, J. C. Derber, R. Treadon, W.-S. Wu, and S. Lord, 2009: Introduction of the GSI into the NCEP global data assimilation system. *Wea. Forecasting*, **24**, 1691–1705, <https://doi.org/10.1175/2009WAF2222201.1>.
- Li, X., G. Zhai, S. Gao, and X. Shen, 2015: Decadal trends of global precipitation in the recent 30 years. *Atmos. Sci. Lett.*, **16**, 22–26, <https://doi.org/10.1002/asl2.514>.
- Lin, S., 2004: A “vertically Lagrangian” finite-volume dynamical core for global models. *Mon. Wea. Rev.*, **132**, 2293–2307, [https://doi.org/10.1175/1520-0493\(2004\)132<2293:AVLFDC>2.0.CO;2](https://doi.org/10.1175/1520-0493(2004)132<2293:AVLFDC>2.0.CO;2).
- , and R. B. Rood, 1996: Multidimensional flux-form semi-Lagrangian transport schemes. *Mon. Wea. Rev.*, **124**, 2046–2070, [https://doi.org/10.1175/1520-0493\(1996\)124<2046:MFFSLT>2.0.CO;2](https://doi.org/10.1175/1520-0493(1996)124<2046:MFFSLT>2.0.CO;2).
- Lin, Y.-L., R. D. Farley, and H. D. Orville, 1983: Bulk parameterization of the snow field in a cloud model. *J. Climate Appl. Meteor.*, **22**, 1065–1092, [https://doi.org/10.1175/1520-0450\(1983\)022<1065:BPOTSF>2.0.CO;2](https://doi.org/10.1175/1520-0450(1983)022<1065:BPOTSF>2.0.CO;2).
- Liu, Y., Z. Tan, and Z. Wu, 2021: Enhanced feedback between shallow convection and low-level moisture convergence leads to improved simulation of MJO eastward propagation. *J. Climate*, **35**, 591–615, <https://doi.org/10.1175/JCLI-D-20-0894.1>.
- Lord, S. J., 1978: Development and observational verification of a cumulus cloud parameterization from the anvil clouds of deep tropical convection. Ph.D. dissertation, University of California, Los Angeles, 359 pp.
- Lorenz, E. N., 1969: Predictability of a flow which possesses many scales of motion. *Tellus*, **21**, 289–307, <https://doi.org/10.3402/tellusa.v21i3.10086>.
- Louf, V., C. Jakob, A. Protat, M. Bergemann, and S. Narsey, 2019: The relationship of cloud number and size with their large-scale environment in deep tropical convection. *Geophys. Res. Lett.*, **46**, 9203–9212, <https://doi.org/10.1029/2019GL083964>.
- Maloney, E. D., and D. L. Hartmann, 2001: The Madden-Julian oscillation, barotropic dynamics, and North Pacific tropical cyclone formation. Part I: Observations. *J. Atmos. Sci.*, **58**, 2545–2558, [https://doi.org/10.1175/1520-0469\(2001\)058<2545:TMJOB>2.0.CO;2](https://doi.org/10.1175/1520-0469(2001)058<2545:TMJOB>2.0.CO;2).
- Mapes, B. E., and R. Neale, 2011: Parameterizing convective organization to escape the entrainment dilemma. *J. Adv. Model. Earth Syst.*, **3**, M06004, <https://doi.org/10.1029/2011MS000042>.
- , S. Tulich, J. L. Lin, and P. Zuidema, 2006: The mesoscale convection life cycle: Building block or prototype for large scale tropical waves? *Dyn. Atmos. Oceans*, **42**, 3–29, <https://doi.org/10.1016/j.dynatmoce.2006.03.003>.
- Matsuno, T., 1966: Quasi-geostrophic motions in the equatorial area. *J. Meteor. Soc. Japan*, **44**, 25–43, [https://doi.org/10.2151/jmsj1965.44.1\\_25](https://doi.org/10.2151/jmsj1965.44.1_25).
- Monahan, A. H., and J. Culina, 2011: Stochastic averaging of idealized climate models. *J. Climate*, **24**, 3068–3088, <https://doi.org/10.1175/2011JCLI3641.1>.
- Moncrieff, M. W., C. Liu, and P. Bogenschutz, 2017: Simulation, modeling, and dynamically based parameterization of organized tropical convection for global climate models. *J. Atmos. Sci.*, **74**, 1363–1380, <https://doi.org/10.1175/JAS-D-16-0166.1>.
- Pan, H.-L., and W.-S. Wu, 1995: Implementing a mass flux convective parameterization package for the NMC medium-range forecast model. NOAA/NMC Office Note 409, 40 pp., <https://repository.library.noaa.gov/view/noaa/11429>.
- Park, S., 2014: A unified convection scheme (UNICON). Part I: Formulation. *J. Atmos. Sci.*, **71**, 3902–3930, <https://doi.org/10.1175/JAS-D-13-0233.1>.
- Plant, R. S., and G. C. Craig, 2008: A stochastic parameterization for deep convection based on equilibrium statistics. *J. Atmos. Sci.*, **65**, 87–105, <https://doi.org/10.1175/2007JAS2263.1>.
- , L. Bengtsson, and M. A. Whitall, 2015: Stochastic aspects of convective parameterization. *Parameterization of Atmospheric Convection. Vol. 2: Current Issues and New Theories*, R. S. Plant and J.-I. Yano, Eds., World Scientific, 135–172.
- Rashid, H. A., H. H. Hendon, M. C. Wheeler, and O. Alves, 2011: Prediction of the Madden-Julian oscillation with the POAMA dynamical prediction system. *Climate Dyn.*, **36**, 649–661, <https://doi.org/10.1007/s00382-010-0754-x>.
- Sakradzija, M., A. Seifert, and A. Dipankar, 2016: A stochastic scale-aware parameterization of shallow cumulus convection across the convective gray zone. *J. Adv. Model. Earth Syst.*, **8**, 786–812, <https://doi.org/10.1002/2016MS000634>.
- Schiro, K. A., S. C. Sullivan, Y. Kuo, H. Su, P. Gentine, G. S. Elsaesser, J. H. Jiang, and J. D. Neelin, 2020: Environmental controls on tropical mesoscale convective system precipitation intensity. *J. Atmos. Sci.*, **77**, 4233–4249, <https://doi.org/10.1175/JAS-D-20-0111.1>.
- Schreck, C. J., J. M. Cordeira, and D. Margolin, 2013: Which MJO events affect North American temperatures? *Mon. Wea. Rev.*, **141**, 3840–3850, <https://doi.org/10.1175/MWR-D-13-00118.1>.
- Siebesma, P., P. M. M. Soares, and J. Teixeira, 2007: A combined eddy-diffusivity mass-flux approach for the convective boundary layer. *J. Atmos. Sci.*, **64**, 1230–1248, <https://doi.org/10.1175/JAS3888.1>.
- Simpson, J., and V. Wiggert, 1969: Models of precipitating cumulus towers. *Mon. Wea. Rev.*, **97**, 471–489, [https://doi.org/10.1175/1520-0493\(1969\)097<0471:MOPECT>2.3.CO;2](https://doi.org/10.1175/1520-0493(1969)097<0471:MOPECT>2.3.CO;2).
- Termonia, P., and Coauthors, 2018: The ALADIN System and its canonical model configurations AROME CY41T1 and ALARO CY40T1. *Geosci. Model Dev.*, **11**, 257–281, <https://doi.org/10.5194/gmd-11-257-2018>.
- Tompkins, A. M., 2001: Organization of tropical convection in low vertical wind shears: The role of cold pools. *J. Atmos. Sci.*, **58**, 1650–1672, [https://doi.org/10.1175/1520-0469\(2001\)058<1650:OOTCIL>2.0.CO;2](https://doi.org/10.1175/1520-0469(2001)058<1650:OOTCIL>2.0.CO;2).
- Tulich, S., and B. E. Mapes, 2010: Transient environmental sensitivities of explicitly simulated tropical convection. *J. Atmos. Sci.*, **67**, 923–940, <https://doi.org/10.1175/2009JAS3277.1>.
- Wheeler, M. C., and G. N. Kiladis, 1999: Convectively coupled equatorial waves: Analysis of clouds and temperature in the wavenumber–frequency domain. *J. Atmos. Sci.*, **56**, 374–399, [https://doi.org/10.1175/1520-0469\(1999\)056<0374:CCEWAO>2.0.CO;2](https://doi.org/10.1175/1520-0469(1999)056<0374:CCEWAO>2.0.CO;2).
- , and H. H. Hendon, 2004: An all-season real-time multivariate MJO index: Development of an index for monitoring and prediction. *Mon. Wea. Rev.*, **132**, 1917–1932, [https://doi.org/10.1175/1520-0493\(2004\)132<1917:AARMMI>2.0.CO;2](https://doi.org/10.1175/1520-0493(2004)132<1917:AARMMI>2.0.CO;2).
- Wu, C., and A. Arakawa, 2014: A unified representation of deep moist convection in numerical modeling of the atmosphere. Part II. *J. Atmos. Sci.*, **71**, 2089–2103, <https://doi.org/10.1175/JAS-D-13-0382.1>.
- Yanai, M., S. Esbensen, and J.-H. Chu, 1973: Determination of bulk properties of tropical cloud clusters from large-scale heat and moisture budgets. *J. Atmos. Sci.*, **30**, 611–627, [https://doi.org/10.1175/1520-0469\(1973\)030<0611:DOBPOT>2.0.CO;2](https://doi.org/10.1175/1520-0469(1973)030<0611:DOBPOT>2.0.CO;2).
- Zhang, C., 2005: Madden-Julian Oscillation. *Rev. Geophys.*, **43**, RG2003, <https://doi.org/10.1029/2004RG000158>.